A Machine Vision Enabled Implantable pH Sensing Scheme Using Ultrasonic Images of Microcomposite Hydrogels

Changqing Guo, Yike Wu, Yi Ma, and Hongjie Jiang, *Member, IEEE*

***Abstract*—Stimuli-responsive hydrogels with embedded microparticles (i.e., silica beads) can be implanted either subcutaneously or deeply to monitor the physiological signals under the epidermis in a remote manner. This can be achieved by using an ultrasonic imaging system to detect the gel deformation in response to the signal change. Unfortunately, it is practically difficult to detect the swelling dynamics of the gel accurately due to the misalignment of the gel and ultrasonic wave. To address this problem, a machine vision-based algorithm is developed. Its procedure is to process the recorded 3-D ultrasonic video using noise reduction, mathematical morphology, edge detection, polygonal approximation, and projection correction, in series. The gel's irregular cross section is then converted to a square, allowing for the accurate determination of its cross-sectional area. In the end, a linear or logarithmic regression model is trained to couple the cross-sectional area of the gel to its surrounding pH value. The optimal result shows the highest R^2 of 0.86 and the lowest RMSE of 0.97. This technique is expected to work with a variety of implantable, wireless hydrogel sensors featuring a portable ultrasonic imaging device.**

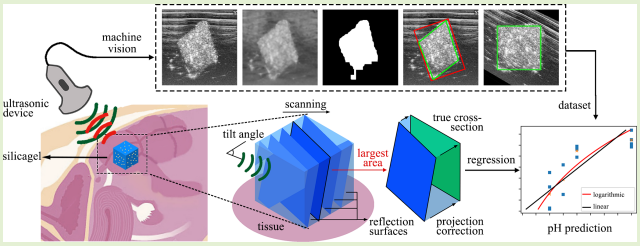

***Index Terms*—Image processing, machine vision, pH sensor, stimuli-responsive hydrogel, ultrasonic imaging.**

I. Introduction

As an alternative to the traditional electrochemical sensing element, environmentally responsive hydrogel-based sensing techniques have received significant scientific attention recently [1], [2], [3]. These responsive polymers exhibit reversible swelling/deswelling behavior in response to environmental stimuli, such as pH [4], temperature [5], and the presence of glucose [6]. Because of this, these hydrogels can be engineered and integrated into a wide range of bioinspired microelectromechanical system (MEMS) applications, including sensors [7], [8], [9], actuators [10], and drug delivery systems [11], [12], [13]. Particularly, compared with wearable sensing, hydrogels or hydrogel-based microdevices have been proven more beneficial for implantable or ingestible devices due to their natural biocompatibility [12]. For example, a research team from the University of Utah achieved mini-invasive continuous glucose monitoring (CGM) by detecting the variation in resonance frequency of an RF oscillator integrated with a glucose-sensitive hydrogel. Its deformation is regulated by the physiological glucose level. With a low-power ASIC, this device enabled a 60-day implanted operation at a 2-cm distance with a transmission efficiency of 5.3% at 6.78 MHz [14]. A more compact CGM scheme used battery-free, passive *LC* resonators, offering capacitances and resonance frequencies shift in response to the changes in the osmotic pressure [7] or the dielectric property of the system when the embedded glucose-responsive hydrogels swell/shrink in response to the increase/decrease of environmental glucose concentration [15]. Another design of *LC* glucose sensors was to modulate the frequency of backscattered signal changes according to the emission light intensity by employing a glucose-responsive fluorescent monomer [16]. In summary, these wirelessly enabled powering and communication devices used the chemomechanical transduction of environmentally sensitive hydrogels to convert chemical signals (e.g., glucose level) into mechanical signals (e.g., pressure or volume change). These wireless systems offer

Manuscript received 20 July 2023; revised 28 August 2023; accepted 27 September 2023. Date of publication 16 October 2023; date of current version 14 November 2023. This work was supported in part by the National Natural Science Foundation of China under Grant 42177440; and in part by The Opening Project of Key Laboratory of Polymer Processing Engineering (South China University of Technology), Ministry of Education, under Grant KFKT2105. The associate editor coordinating the review of this article and approving it for publication was Prof. Chao Tan. *(Corresponding author: Hongjie Jiang.)*

The authors are with the Shien-Ming Wu School of Intelligent Engineering, South China University of Technology, Guangzhou 511442, China (e-mail: jiang1029@scut.edu.cn).

Digital Object Identifier 10.1109/JSEN.2023.3323558

the fundamental advantages of avoiding tissue pricking and minimizing danger and agony for patients, when compared with traditional wired detection devices. However, one of their primary drawbacks is the limited telemetry distance. The active sensors energized by RF are normally limited to 2-cm distance [17], and passive sensors based on near-field communication (NFC) typically operate below the skin at the millimeter scale [15], both of which are incapable of deep implantation.

To avoid such shortcomings, our previous works developed a pH-sensitive microcomposite hydrogel by embedding microsilica beads into the polymeric network named Silica gel. Its volumetric change (i.e., its cross-sectional area) in response to chemical stimuli, such as pH value, is captured using an ultrasound imaging system to quantify the environmental pH. The technology eliminates one of the main obstacles in wireless passive sensing because ultrasonic waves at clinical imaging frequencies (2–20 MHz) can penetrate deep tissue (>10 cm). Besides, we have two additional works that apply the same idea. One developed a highly stretchable hydrogel embedded with (ZnO) nanoparticles, which served as an ideal biocompatible ultrasound contrast agent that allows remote interrogation of the changes in volume or dimensions of the hydrogel in response to mechanical strains, when attached to an abdominal organ [18]. The other created a pressure-sensitive implanted microfluidic transducer with a water reservoir and a hydrophobic microchannel attached to it. By keeping track of the water's progress through the channel, it was able to measure the applied pressure. This technology enabled a broad range of implantable pressure measurements [19].

This method correlates the cross-sectional area of the silica gel sample to its surrounding pH level. In this detection system, the ultrasound emission wave must be in a plane with the gel's cross section. Only, then, the gel deformation and, thus, the pH value of the environment can be measured accurately. However, it is practically challenging to meet these criteria. Once implanted subcutaneously, the gel could spin or tilt. However, even a slight rotation or movement could cause the ultrasound wave to move out of the plane with the gel's cross section. Such a misalignment will cause an incorrect reading of the cross-sectional area and, concurrently, a failure of pH detection.

As a follow-up to the earlier research, we developed a machine vision-based implantable, wireless pH sensing system by employing the 3-D ultrasonic images of silica gel, as shown in Fig. 1. In this work, we concentrate on the real-time image processing for each frame of the recorded ultrasonic video during the swelling/deswelling of the silica gel in response to the surrounding pH level. Combining machine vision and regression analysis, one can extract the true gel deformation and determine the corresponding pH value.

II. Methodologies

Fig. 2 depicts the methodologies. Due to the unevenness of the human tissues, superimposed scattering waves from the ultrasonic echo produce different types of image noises, including salt and pepper noise, stripe noise, and random noise. A set of different noise reduction methods are conducted. Salt and pepper noises are reduced by employing kernel methods, e.g., median filtering. Stripe noises are reduced by converting the image to gray scale and applying a convolution in the Fourier domain. The random noises are reduced by morphological methods, such as dilating and eroding with tuned iteration and range. After noise reduction, the edge-following algorithm processes each frame of the 3-D ultrasonic video to recognize the gel edge. Then, a quadrilateral/rectangular approximation (RA) method was applied to fit any rotated section of the gel to a polygonal shape. The polygonal was then converted to a standard square to recover the image with the largest cross-sectional area of the gel via a vector calculation-based projection correction. Finally, a trained linear/logarithmic model is employed to evaluate and predict the surrounding pH level in terms of RMSE and R^2.

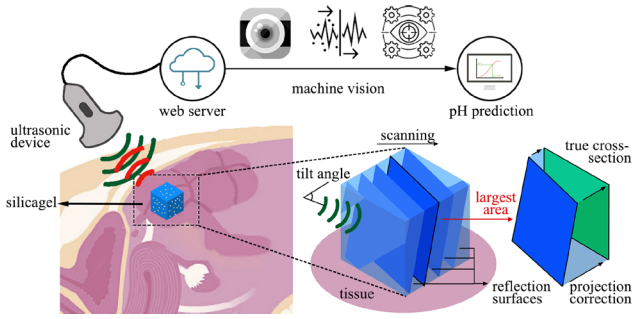

Fig. 1. Schematic of the machine vision-assisted silica gel sensor using a portable ultrasonic imaging device. The principle is to develop and apply a set of ultrasonic image process techniques to accurately measure the gel's volumetric deformation in terms of its cross-sectional area change and consequently predict the surrounding pH change.

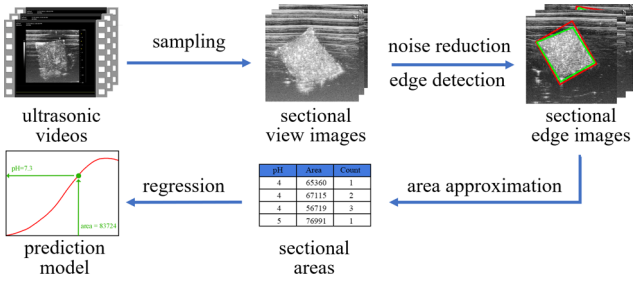

Fig. 2. Developed algorithm of image processing based on machine vision, including sampling, noise reduction, edge detection, approximation, projection, and regression.

A. Noise Reduction

Salt and pepper noise usually appears as isolated bright or dark pixels in the image due to data acquisition or transmission when the ultrasonic wave travels through the gel network or the surrounding medium (e.g., human tissue). It can be reduced by applying nonlinear filtering methods, like order-statistic filters [17]. Thus, a median filter with a kernel size of 15 pixels × 15 pixels is first used to remove salt and pepper noises in the obtained ultrasonic images.

Along-track stripe noises are a common problem in ultrasonic images and they are mainly caused by the movement of the ultrasonic beam, resulting in an overlap or shift of the ultrasonic wave beam. Along-track stripe noises can be reduced by using a Fourier transform to transfer the image from the spatial

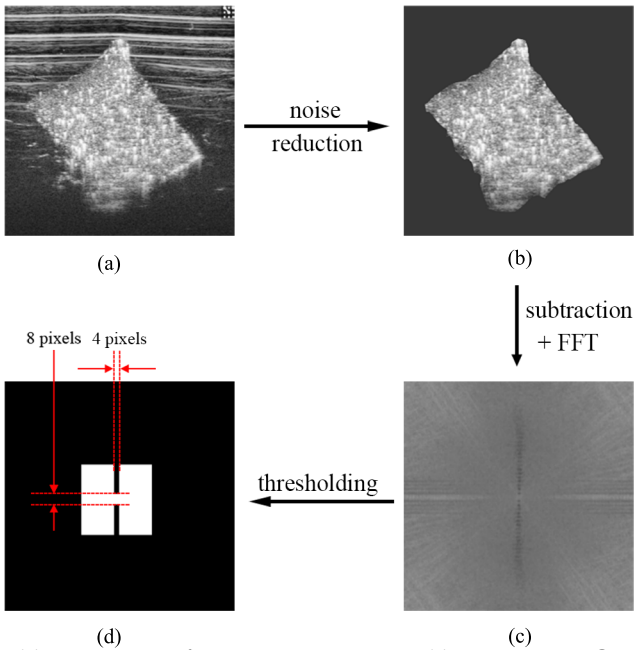

Fig. 3. Illustration of the process to obtain the FFT convolution mask. (a) Original image. (b) Ideal result. (c) Convolutional layer. (d) Difference image.

domain to the frequency domain and applying a convolution operation to the transformed image [15], [17]. Fig. 3 illustrates the development process of the convolution layer. At first, the original image was filtered using a programed edge detection technique to turn all of the pixels outside the gel black. This produced an image with no noise [Fig. 3(a) and (b)]. Then, the noise-free image was subtracted from the original image in the Fourier domain to obtain a different image. Next, the convolutional layer was generated by applying a thresholding to the difference image. In thresholding, the central one-ninth of the convolution layer serves as a low-pass filter, with two narrow, vertical indentations of 4 pixels wide set to black, leaving a white window of 4 pixels × 8 pixels (width × length) at the center [Fig. 3(c) and (d)]. At last, the original image was convoluted and then used reverse fast Fourier transform (FFT) to create a gray-scale image.

Random noise could be caused by the presence of air bubbles entrapped in the medium mimicking human tissue or the nonuniform distribution of silica beads embedded in the hydrogel. In an ultrasonic image, the former produces large spots appearing as bright pixels, while the latter generates large cavities appearing as dark pixels. Both of them will cause large scattering or attenuation of the ultrasonic wave, thus affecting the image quality. Unlike salt and pepper noise or stripe noise, random noise is difficult to be reduced by conventional filtering techniques but can be reduced by morphology methods [18]. In the process, the original images are first binarized and then applied with either open operation (i.e., erosion followed by dilation) to remove spots or close operation (i.e., dilation followed by erosion) to fill cavities. The operation window is set to 5 pixels deep and the iteration is set to two times.

Three indices were calculated to evaluate the result of noise reduction, including mean square error (MSE), peak signal-to-noise ratio (PSNR), and structural similarity (SSIM). MSE is measured by the following equation:

$$\mathrm{MSE} = \frac{1}{mn}\sum_{i=0}^{m-1}\sum_{j=0}^{n-1}\left[I\,(i,\,j) - K\,(i,\,j)\right]^2 \tag{1}$$

where m and n are the image sizes, I and K stand for the test image and the noise-free image at a gray level from 0 to 255, respectively, and i and j are the pixel coordinates. Lower MSE, less noise, and thus, better image quality.

PSNR is a measure of the ratio between the maximum possible magnitude of the pixel of an image and that of the noise, defined by the following equation:

$$\mathrm{PSNR} = 20\log_{10}\left(\frac{\mathrm{MAX}_i}{\sqrt{\mathrm{MSE}}}\right) \tag{2}$$

where MAX_i is the maximum value (e.g., 255 for an 8-bit gray-scale image) of the ith image. Larger PSNR, better image quality.

SSIM measures image similarity in luminance, contrast, and structure as a fully referenced image quality evaluation metric [19], defined as follows:

$$\mathrm{SSIM}(X,\,Y) = \frac{(2\mu_x\mu_y + C_1)(2\delta_{xy} + C_2)}{\left(\mu_x^2\mu_y^2 + C_1\right)\left(\delta_x^2\delta_y^2 + C_2\right)} \tag{3}$$

where X and Y are the compared images, μ_x and μ_y are the average values of X and Y, δ_x and δ_y are their standard deviation, δ_{xy}^2 is the covariance, and C_1 and C_2 are the constants to avoid numerical instability. At a range of 0–1, a larger SSIM indicates less image distortion.

B. Edge Detection

Edges are expressed as discrete pixels in a binarized image [20], [21], which can be detected using topological structural analysis by border following. In this study, open-source computer vision library (OpenCV) is used to identify the edges in the processed image following the noise reduction. In 1999, the Intel team released the OpenCV to advance vision research, disseminate vision knowledge, and create a library of programming functions with optimized and portable code. By selecting the size and shape of the neighborhood (i.e., structural elements), OpenCV can implement morphological operations sensitive to specific shapes in the input image [22].

To increase the robustness of edge detection, polygonal approximation methods are applied to process the discrete result by OpenCV. Since the gel is patterned in the form of a cube, the gel that swells or shrinks in response to the increase or decrease of the surrounding pH should also be in the shape of a cube, given that the gel deforms isotropically. In this regard, the edge pixels were approximately fit to continuous line segments, whereas the gel shape was fit into a quadrilateral or rectangular frame to prevent overfitting. For quadrilateral approximation (QA), the Douglas–Peucker Algorithm [23] is employed with the key parameter, i.e., the maximum distance between the original curve and its approximation, set to be 0.02, 0.08, and 0.15 times of the edging perimeter. Whereas for RA, the rotating calipers algorithm is adopted to obtain the minimum area of the circumscribed rectangle as the approximated frame.

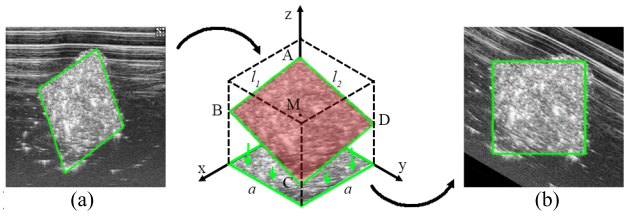

Fig. 4. Projection correction illustration. (a) Original image is distorted due to the misalignment between the gel and ultrasonic wave and (b) corrected cross section is acquired in a form of a square by projection correction.

C. Projection Correction

After the edge detection, one is able to acquire any of the gel's sectional areas in the plane with the emissive ultrasonic wave. To obtain the correct cross-sectional area of the gel by eliminating the effects of gel rotation or tilt, projection correction is required. This process is depicted in Fig. 4. When the ultrasonic wave travels through the centroid of a cubical gel with a width of a at an inclined angle of θ to the gel top surface, the gel section with the maximum area would appear in the shape of a parallelogram [Fig. 4(a)]. From the image analysis, one is able to measure the lengths of the two edges (defined as l_1 and l_2, respectively) and the area (defined as s) of the parallelogram. Thus, the projection correction is to obtain the gel width (i.e., a) from l_1, l_2, and s. By doing so, we can apply a simple square area equation to calculate the true cross-sectional area (i.e., a^2) of the gel and correlate it to the pH value.

The following formulas are used to determine a parallelogram's square area. In XYZ space, the normal vector of the parallelogram (indicated as red in Fig. 4) is defined as $\vec{e} = (i, j, k)$, and the coordinates of its four corners (i.e., A–D) are defined as $(0, 0, z_{00})$, $(0, a, z_{0a})$, $(a, 0, z_{a0})$, and (a, a, z_{aa}), respectively. Next, the point at the intersection between the parallelogram and the center axis of the gel is defined as $[(a/2), (a/2), z_0]$. Then, the Z-coordinates of the parallelogram's four corners can be written as the function of the gel width, the normal vector, and the parallelogram's centric point as follows:

$$\text{plane } ABCD:\ i\left(x-\frac{a}{2}\right)+j\left(y-\frac{a}{2}\right)+k\left(z-z_0\right)=0 \tag{4}$$

$$z_{pq}=z_0+\frac{a}{2k}\left((-1)^{p/a}i+(-1)^{q/a}j\right),\quad p \text{ or } q=0 \text{ or } a \tag{5}$$

and the lengths of the parallelogram's edges can be described as follows:

$$\begin{aligned} l_1 &= |z_{00}z_{01}| = |z_{10}z_{11}| = a\sqrt{1+i^2/k^2} \\ l_2 &= |z_{01}z_{11}| = |z_{10}z_{00}| = a\sqrt{1+j^2/k^2}. \end{aligned} \tag{6}$$

These equations allow for the mapping of the gel section from the XYZ space to the XY plane, as shown in Fig. 4(b). Afterward, the square cross-sectional area a^2 of the gel can be expressed as the function of the parallelogram's edges and area as follows:

$$a^2 = 0.5\left(\left(l_1^2+l_2^2\right)-\sqrt{\left(l_1^2+l_2^2\right)^2-4S^2}\right). \tag{7}$$

D. Regression and Prediction

The calibration curves between gel cross-sectional areas and pH values are investigated using regression methods, including linear regression and logarithmic regression. The linear regression is performed using least square fitting [25] as follows.

Do regression on β_0, β_1

$$\begin{aligned} &\min\ (\mathrm{pH}_i-(\beta_0+\beta_1 S))^2 \\ &\text{constrain: } \widehat{\mathrm{pH}}_{\mathrm{fit}}=\beta_0+\beta_1 S. \end{aligned}$$

Find the outliers of pH_i

$$\text{If } |\mathrm{pH}_i-(\beta_0+\beta_1 S)|\geq 5,\quad \text{then outlier} = \text{TRUE}.$$

Remove the outliers and continue the regression.

In the pseudocodes, pH_i is defined as the true value of surrounding pH, $\widehat{\mathrm{pH}}_{\mathrm{fit}}$ is defined as the modeled value, and β_0 and β_1 are the two parameters of the modeled linear function between pH values and gel cross-sectional areas, S.

RMSE and R^2 were used to evaluate the accuracy and degree of discreteness of the two calibration curves [25]. R-squared is an indicator of the fitting degree between the estimated and actual values. The higher the R-squared value, the higher the reliability of the predictive model. Meanwhile, root-mean-square error (RMSE) measures the deviation between the predicted and true values. The lower the RMSE, the better the performance of the predictive model. The following equations show the computational formulas:

$$\mathrm{RMSE}=\sqrt{\frac{1}{N}\sum_{i=1}^{N}\left(\widehat{\mathrm{pH}}_{\mathrm{fit}}-\mathrm{pH}_i\right)^2} \tag{8}$$

$$R^2=1-\frac{\sum_i\left(\widehat{\mathrm{pH}}_{\mathrm{fit}}-\mathrm{pH}_i\right)^2}{\sum_i\left(\overline{\mathrm{pH}}-\mathrm{pH}_i\right)^2}. \tag{9}$$

III. Experiments

The pH-sensitive silica gel was fabricated to be in the form of a cube with 2-mm width and 10% w/w silica beads (9–13-μm diameter) using the previously reported method [13]. After synthesis, hydrogels were transferred onto a layer of agarose gel and covered with 10-mm-thick porcine skin tissue. Vevo2100 ultrasound imaging system (VisualSonics) with a 40-MHz transducer (MS550D, MicroscanTM Transducers) was used to produce the 3-D images of the hydrogel. Before describing silica gel as a function of pH, the silica gel was immersed in a pH solution for one day to achieve its equilibrium. Four different pH solutions were used as pH 4–6 and 10.

The work generated 17 videos, each of which had a scan rate of 5 frames/s, lasted 20 s, and contained 100 total frames. Each frame is 450 pixels × 450 pixels in height and width. Prior to the process, the captured video was converted to gray scale and sampled at a sampling rate of 2 frames/s (i.e., 40 frames per

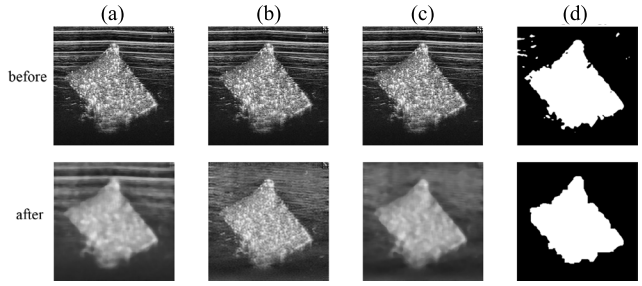

Fig. 5. Photographs of the effects of applying different noise reduction methods, including (a) median filter, (b) filter in Fourier domain, (c) median followed by FFT, and (d) mathematical morphology, to the same image sample.

video). Then, these frames were analyzed by machine vision methods described previously. In the analysis, five combinations were evaluated in terms of R^2 and RMSE, including raw edge, QA, QA + projection correction, RA, and RA + projection correction. Raw Edge refers to the application of only edge detection without QA/RA and projection correction of the image, whereas RA refers to the application of only RA without projection correction of the image. Python 3.8 was used for the coding.

IV. Results and Discussion

A. Noise Reduction

Fig. 5(a) shows the reduction of salt and pepper noises from a sample image using the median filter with a 15 pixels × 15 pixels kernel. In the processed image, spot noises that appear as the bright isolated pixels in and out of the gel contour were greatly canceled. Stripe noises in the upper areas of the image were also filtered in terms of blurring. Moreover, the image edges were well preserved without being distorted.

Fig. 5(b) shows the reduction of stripe noises from the same image by applying a convolution calculation in the Fourier domain. The stripe noises in the upper areas of the image were reduced significantly, while the bright isolated pixels inside the gel were well preserved. Since the convolution layer contains a low-pass filter, the image was blurred slightly. It can be seen that filtering in the Fourier domain decreases stripe noise with less loss in sharpness, when compared to using a median filter.

The use of combining different filers to process the image was also investigated, i.e., conducting the median filter and FFT in series. The result is shown in Fig. 5(c). When compared with employing FFT alone, salt and pepper noises as well as stripe noises were both significantly diminished. After being binarized, the filtered image was further processed using the mathematical morphology method to simplify the structure of the gel. As shown in Fig. 5(d), large spot noises, or random noises, were reduced, and the edges appeared smoother, when compared to that by using edge detection without mathematical morphology [the upper figure in Fig. 5(d)].

The effects of noise reduction were also illustrated in the histograms. In the raw image, 95% of pixels at a range of 31–210 [Fig. 6(a)] were reallocated to that of 38–192 (95%) using a median filter [Fig. 6(b)]. This is due to the fact that salt and pepper noises of the image typically appear as discrete bright pixels with high gray values (e.g., larger than 192), the

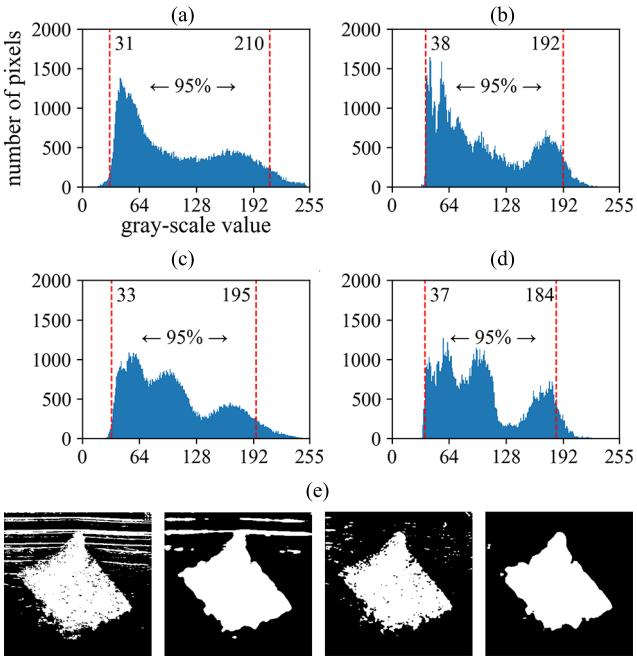

Fig. 6. Histogram of the selected raw image in 0–255 gray scale (a) before and (b)–(d) after the application of different noise reduction as well as (e) binarized images.

TABLE I
PSNR, SSIM, and MSE Results of Three Noise Reduction Methods

	MSE	PSNR	SSIM
Median Filter	1103	17.71	0.54
FFT	879	18.69	0.58
Median Filter + FFT	879	18.69	0.62

reduction of which cause these filtered pixels to shift to lower ones. Using a filter in the Fourier domain [Fig. 6(c)], on the other hand, it was observed that a large number of pixels moved from below 64 to the range of 64–128 with a peak occurring at a gray value of approximately 100. Meanwhile, the envelope of its histogram became smooth. This resulted from the convolution mask's low-pass filtering effects on the stripe noises. Thus, it is expected that combining the two types of filters will reshape the histogram into one that is more informative. As shown in Fig. 6(d), a valley emerged at a gray value of 128, which indicated a distinct boundary between the silica gel (with pixels larger than 128) and the background (with pixels smaller than 128). More importantly, the threshold for binarizing and then using the morphology method might be set at 128 or a small range around 128, respectively. As a result, the processed image's binarization will have a clear contour free of noise [the fourth subfigure of Fig. 6(e)]; otherwise, it will have a significant amount of noise in the background, or in the gel, or both [the first three subfigures of Fig. 6(e)].

The quantitative analysis of noise reduction was evaluated by comparing the processed images to the noise-free ones [Fig. 3(b)] and calculating MSE, PSNR, and SSIM, as shown in Table I. The median filter obtained an MSE of 1103 and

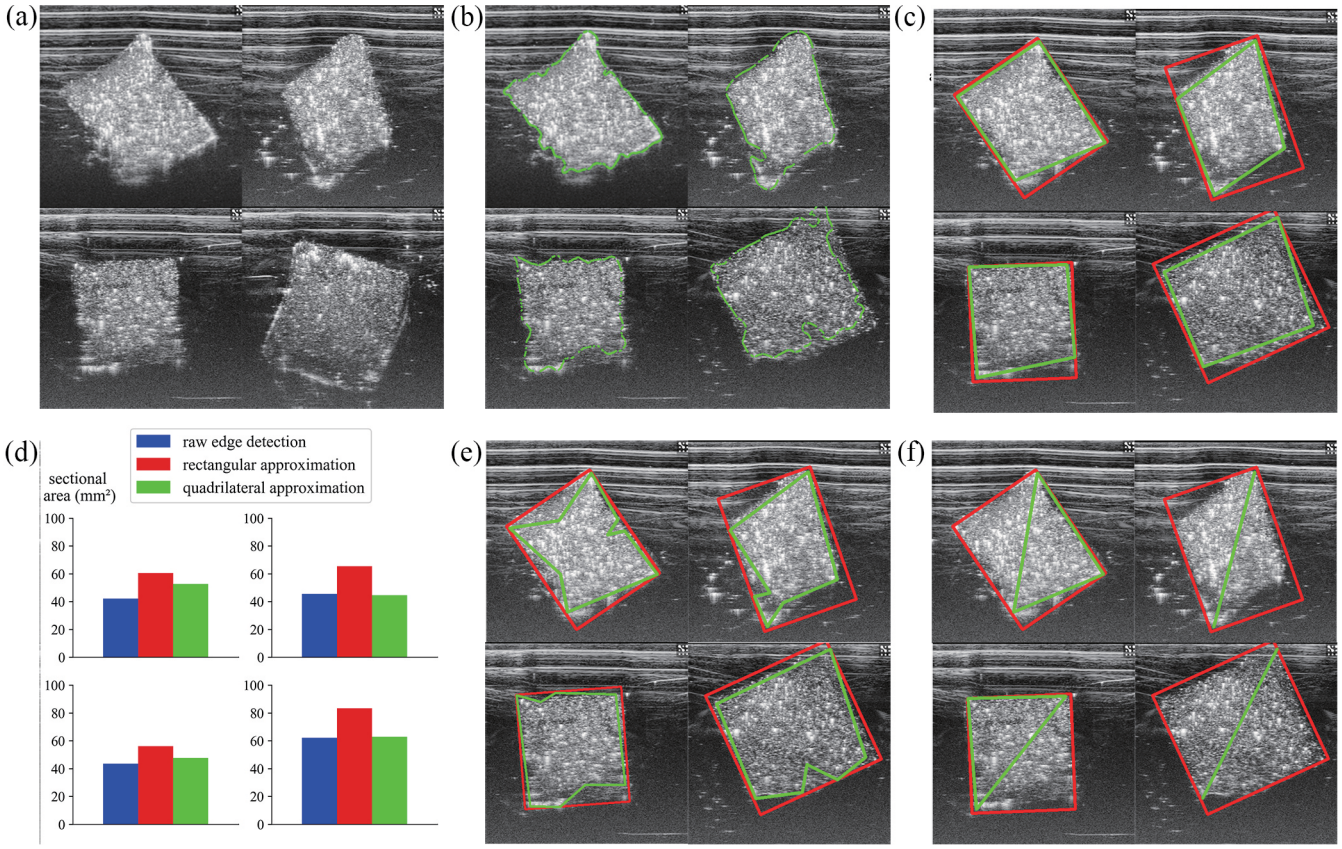

Fig. 7. (a) Four types of irregular shapes of ultrasonically imaged gels applied with edge detection and (b) without and (c) with polygonal approximations (e.g., quadrilateral (green) and rectangular (red) approximation), and (d) detected sectional area by different methods was compared. The maximum distance between the original curve and its approximation is set as 0.08 times the edging perimeter. Other results using (e) 0.02 and (f) 0.15 times the edging perimeter.

PSNR of 17.71 dB, respectively. These values are 1.25 and 0.95 times those of 879 (MSE) and 18.69 dB (PSNR) by using FFT or median filter + FFT. The comparison showed that strip noises predominated and had a greater impact on the ultrasonic images than salt and pepper noises did. As a result, the image quality was improved by removing the strip noises. On the other hand, combining the Median filter and FFT achieved the largest SSIM value, which is 0.62, 1.07, or 1.15 times that of using FFT or median filter individually. Because different noise types would affect the total index differently and due to the fact that the SSIM value measures the structural similarity between the processed and noise-free image, a combination of different filters produces the highest SSIM.

B. Edge Detection

After noise reduction, we performed edge detection and polygonal approximation using OpenCV. Four typical types of raw images with irregular shapes were selected and processed [Fig. 7(a)]. Fig. 7(b) shows their detected edges, which are anomalous and discrete, by applying edge recognition alone. These were improved by continuing the image process with approximation methods. As shown in Fig. 7(c), the irregular edges were mapped to either quadrilaterals [green contour in Fig. 7(c)] or rectangles [red contour in Fig. 7(c)]. It was observed that the projected area of the RA is larger than that of raw edge detection or QA [Fig. 7(d)]. For example,

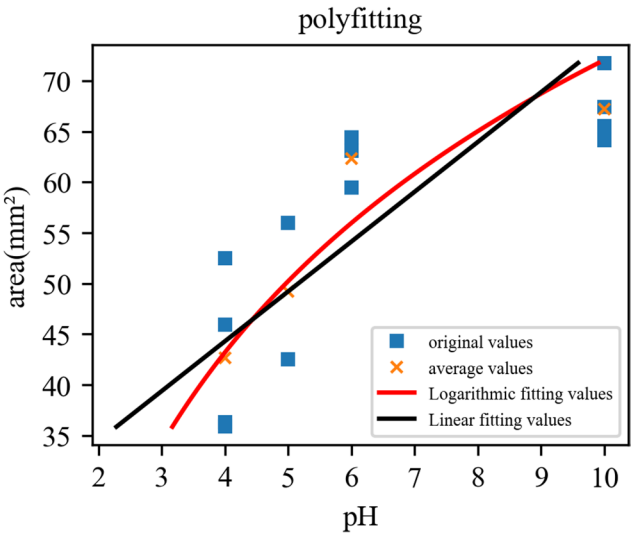

Fig. 8. Gel cross-sectional area as a function of pH using linear or logarithmic regression.

RA measured the area of the projected image at the lower right corner of Fig. 7(c) to be 88 mm^2, which is 1.23 and 1.38 times that of 72 and 64 mm^2 using raw edge detection and QA, respectively. This could lead to an overestimation of the true cross section, which was discussed next in terms of prediction linearity and accuracy. The result shown above was achieved by setting the maximum distance between the

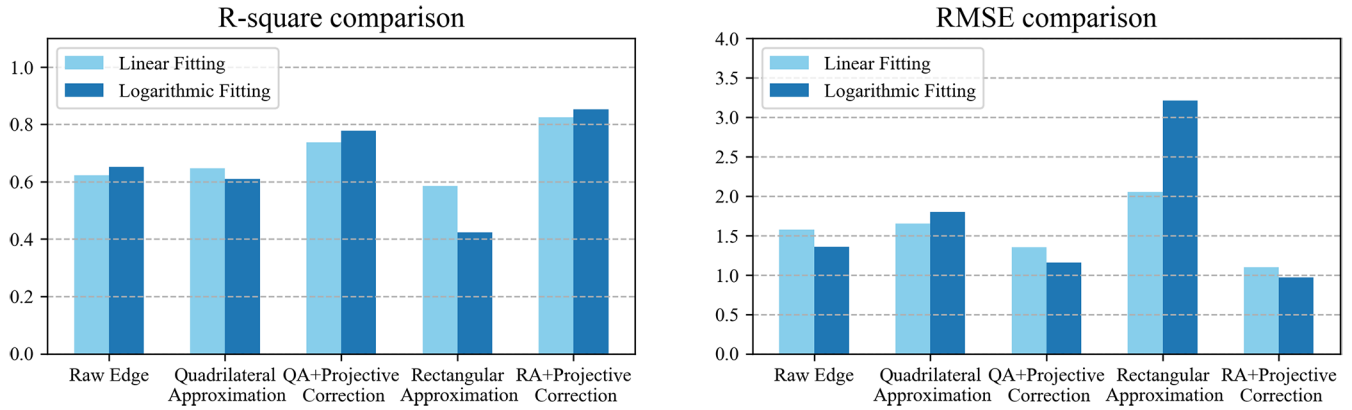

Fig. 9. Comparison of R^2 and RMSE by different machine vision methods combined with regression models.

original curve and its approximation as 0.08 times the edging perimeter. The result of two more criteria, 0.02 or 0.15 times the edging perimeter, was also evaluated. As can be seen from Fig. 7(e) and (f), a smaller threshold would result in under-fitting the irregular edges, leading to a polygon with more than four vertices. Consequently, the projection correction cannot be effectively performed (the former). Conversely, a larger threshold caused overfitting and a bigger generalization error. This would increase the variance of the cross-section area, ultimately decreasing the sensitivity of the sensor (the latter). Overall, the approximation methods provide reliable detection of edges with effective irregularity compensation following noise reduction.

C. Regression and Prediction

After the regression analysis, two calibration curvatures were generated to fit the gel cross-sectional area to the surrounding pH value, as shown in Fig. 8 as follows:

$$\text{area} = 4.92\text{pH}_1 + 24.6 \tag{10}$$

$$\text{area} = 31.5\log_{10}\left(\text{pH}_2\right) + 0.46. \tag{11}$$

Equation (10) describes the area-to-pH relationship using linear regression, whereas (11) writes this using logarithmic regression. It is intriguing to note that the latter has a higher sensitivity of 31.5 mm^2/pH when examining the linearity between area and pH logarithm (instead of pH), which is 6.4 times that of 4.92 mm^2/pH of the former. In this regard, it is expected that one is able to achieve higher prediction quality using logarithmic regression.

D. Evaluation

To determine the correct cross-sectional area of the gel, five combinations of approximation and projection methods are applied, and their effects are evaluated. The results are shown in Fig. 9. RA had the smallest R-squared values, 0.58 and 0.42 for linear and logarithmic regressions, respectively, compared to the other four combinations, which all have values greater than 0.6. Meanwhile, RA + projection correction obtained the largest R-squared values, 0.83 and 0.85 for linear and logarithmic regressions, respectively. Therefore, it is reasonable to conclude that the projection correction following the quadrilateral/RA attributes to the increase of the functional linearity between cross-sectional areas and pH values.

In the evaluation of RMSE, a similar pattern was observed. For linear and logarithmic regressions, respectively, RA alone had the highest RMSE of 2.1 and 3.2, while RA + projection correction reduced this to 1.1 and 0.97, respectively. Among the five combinations, these are the smallest. As a result, it could be inferred that RA + projection correction can improve the prediction accuracy. In addition, when RA + projection correction is applied, the logarithmic technique exhibited a slightly larger R-square and a smaller RMSE than the linear regression, indicating that this combination is the best one for fitting the gel area-to-pH curve.

V. Conclusion

In this article, a machine vision-based algorithm is developed to analyze ultrasonic images of silica gel, which swells/shrinks in response to the increase/decrease of pH. This approach begins to reduce different types of noises in the image using a median filter or FFT or both followed by mathematical morphology. Edge detection with a polygonal approximation is then performed to project the irregular shape of the detected gel cross section to be a form of a square. In the end, a mathematical regression method is applied to establish the calibration curve, which is the function of gel cross-sectional area versus pH value. With an optimal combination of image processing techniques and regression methods, the prediction to couple the area to pH achieves a high accuracy of $R^2 = 0.86$ and RMSE = 0.97. This technique approves its practical potential in a variety of implantable, wireless hydrogel sensing using ultrasonic imaging devices to monitor the physiological signals in real time.

References

[1] H. Yuk, B. Lu, and X. Zhao, "Hydrogel bioelectronics," *Chem. Soc. Rev.*, vol. 48, no. 6, pp. 1642–1667, 2019, doi: 10.1039/c8cs00595h.

[2] A. Richter, G. Paschew, S. Klatt, J. Lienig, K.-F. Arndt, and H.-J. Adler, "Review on hydrogel-based pH sensors and microsensors," *Sensors*, vol. 8, no. 1, pp. 561–581, Jan. 2008, doi: 10.3390/s8010561.

[3] H. Yuk, J. Wu, and X. Zhao, "Hydrogel interfaces for merging humans and machines," *Nature Rev. Mater.*, vol. 7, no. 12, pp. 935–952, Oct. 2022, doi: 10.1038/s41578-022-00483-4.

[4] D. Schmaljohann, "Thermo- and pH-responsive polymers in drug delivery," *Adv. Drug Del. Rev.*, vol. 58, no. 15, pp. 1655–1670, Dec. 2006, doi: 10.1016/j.addr.2006.09.020.

[5] S. Hirotsu, Y. Hirokawa, and T. Tanaka, "Volume-phase transitions of ionized N-isopropylacrylamide gels," *J. Chem. Phys.*, vol. 87, no. 2, pp. 1392–1395, Jul. 1987, doi: 10.1063/1.453267.

[6] C. Zhang, M. D. Losego, and P. V. Braun, "Hydrogel-based glucose sensors: Effects of phenylboronic acid chemical structure on response," *Chem. Mater.*, vol. 25, no. 15, pp. 3239–3250, Aug. 2013, doi: 10.1021/cm401738p.

[7] M. Lei, A. Baldi, E. Nuxoll, R. A. Siegel, and B. Ziaie, "A hydrogel-based implantable micromachined transponder for wireless glucose measurement," *Diabetes Technol. Therapeutics*, vol. 8, no. 1, pp. 112–122, Feb. 2006, doi: 10.1089/dia.2006.8.112.

[8] J. H. Holtz and S. A. Asher, "Polymerized colloidal crystal hydrogel films as intelligent chemical sensing materials," *Nature*, vol. 389, no. 6653, pp. 829–832, Oct. 1997, doi: 10.1038/39834.

[9] S. Matsumura et al., "Introduction of pH-sensitivity into mechanically strong nanoclay composite hydrogels based on N-isopropylacrylamide," *Amer. Chem. Soc. Polym. Prepr. Div. Polym. Chem.*, vol. 49, no. 1, pp. 511–512, 2008, doi: 10.1002/pola.22973.

[10] A. Baldi, Y. Gu, P. E. Loftness, R. A. Siegel, and B. Ziaie, "A hydrogel-actuated environmentally sensitive microvalve for active flow control," *J. Microelectromech. Syst.*, vol. 12, no. 5, pp. 613–621, Oct. 2003, doi: 10.1109/JMEMS.2003.818070.

[11] X. Zhao et al., "Active scaffolds for on-demand drug and cell delivery," *Proc. Nat. Acad. Sci. USA*, vol. 108, no. 1, pp. 67–72, Jan. 2011, doi: 10.1073/pnas.1007862108.

[12] Y. Qiu and K. Park, "Environment-sensitive hydrogels for drug delivery," *Adv. Drug Del. Rev.*, vol. 64, pp. 49–60, Dec. 2012, doi: 10.1016/j.addr.2012.09.024.

[13] H. Jiang, M. Ochoa, J. F. Waimin, R. Rahimi, and B. Ziaie, "A pH-regulated drug delivery dermal patch for targeting infected regions in chronic wounds," *Lab Chip*, vol. 19, no. 13, pp. 2265–2274, 2019, doi: 10.1039/c9lc00206e.

[14] D. Wilken, P. Feldens, T. Wunderlich, and C. Heinrich, "Application of 2D Fourier filtering for elimination of stripe noise in side-scan sonar mosaics," *Geo-Marine Lett.*, vol. 32, no. 4, pp. 337–347, Aug. 2012, doi: 10.1007/s00367-012-0293-z.

[15] E. Coello et al., "Fourier domain image fusion for differential X-ray phase-contrast breast imaging," *Eur. J. Radiol.*, vol. 89, pp. 27–32, Apr. 2017, doi: 10.1016/j.ejrad.2017.01.019.

[16] H. J. A. M. Heijmans, "Mathematical morphology: A modern approach in image processing based on algebra and geometry," *SIAM Rev.*, vol. 37, no. 1, pp. 1–36, Mar. 1995, doi: 10.1137/1037001.

[17] A. A. Vassiliou, M. Boulianne, and J. A. R. Blais, "On the application of averaging median filters in remote sensing," *IEEE Trans. Geosci. Remote Sens.*, vol. 26, no. 6, pp. 832–838, Nov. 1988, doi: 10.1109/36.7714.

[18] H. Jiang et al., "A wireless implantable strain sensing scheme using ultrasound imaging of highly stretchable zinc oxide/poly dimethylacrylamide nanocomposite hydrogel," *ACS Appl. Bio Mater.*, vol. 3, no. 7, pp. 4012–4024, Jul. 2020, doi: 10.1021/acsabm.9b01032.

[19] H. Jiang et al., "A wireless implantable passive intra-abdominal pressure sensing scheme via ultrasonic imaging of a microfluidic device," *IEEE Trans. Biomed. Eng.*, vol. 68, no. 3, pp. 747–758, Mar. 2021, doi: 10.1109/TBME.2020.3015485.

[20] A. Hore and D. Ziou, "Image quality metrics: PSNR vs. SSIM," in *Proc. 20th Int. Conf. Pattern Recognit.*, Aug. 2010, pp. 2366–2369, doi: 10.1109/ICPR.2010.579.

[21] V. Torre and T. A. Poggio, "On edge detection," *IEEE Trans. Pattern Anal. Mach. Intell.*, vol. PAMI-8, no. 2, pp. 147–163, Mar. 1986, doi: 10.1109/TPAMI.1986.4767769.

[22] R. Owens, S. Venkatesh, and J. Ross, "Edge detection is a projection," *Pattern Recognit. Lett.*, vol. 9, no. 4, pp. 233–244, 1989, doi: 10.1016/0167-8655(89)90002-0.

[23] A. Sharma, J. Pathak, M. Prakash, and J. N. Singh, "Object detection using OpenCV and Python," in *Proc. 3rd Int. Conf. Adv. Comput., Commun. Control Netw.*, 2021, pp. 501–505, doi: 10.1109/ICAC3N53548.2021.9725638.

[24] A. Saalfeld, "Topologically consistent line simplification with the Douglas–Peucker algorithm," *Cartography Geographic Inf. Sci.*, vol. 26, no. 1, pp. 7–18, Jan. 1999, doi: 10.1559/152304099782424901.

[25] P. Stephen and S. Jaganathan, "Linear regression for pattern recognition," in *Proc. Int. Conf. Green Comput. Commun. Electr. Eng. (ICGCCEE)*, Mar. 2014, pp. 1–6, doi: 10.1109/ICGCCEE.2014.6921393.

Changqing Guo is currently pursuing the B.S. degree with the Shien-Ming Wu School of Intelligent Engineering, South China University of Technology, Guangzhou, China.

Yike Wu is currently pursuing the B.S. degree with the Shien-Ming Wu School of Intelligent Engineering, South China University of Technology, Guangzhou, China.

Yi Ma received the B.S. degree in mechanical manufacturing and automation from the East China University of Science and Technology, Shanghai, China, in 2020. He is currently pursuing the M.S. degree with the Shien-Ming Wu School of Intelligent Engineering, South China University of Technology, Guangzhou, China.

Hongjie Jiang (Member, IEEE) received the Ph.D. degree in electrical and computer engineering with Purdue University, West Lafayette, IN, USA, in 2018.

He is currently an Associate Professor with the Shien-Ming Wu School of Intelligent Engineering, South China University of Technology, Guangzhou, China. His research focuses on the development of stretchable, low-cost, and flexible microsystem platforms for biomedical applications.